
Article:
Vargas-Cardona, H.D., Orozco, A.A., Alvarez, A.M. et al. (1 more author) (2018) Tensor decomposition processes for interpolation of diffusion magnetic resonance imaging. Expert Systems with Applications. ISSN 0957-4174

https://doi.org/10.1016/j.eswa.2018.10.005

Tensor decomposition processes for interpolation of diffusion magnetic resonance imaging

Hernán Darío Vargas-Cardona*[a], Álvaro A. Orozco[a], Andrés M. Álvarez[b], Mauricio A. Álvarez[c]

[a] *Department of Electrical Engineering, Universidad Tecnológica de Pereira, Cra 27 #10 − 02 Barrio Alamos, Pereira, Colombia, 660003,*
E-mail: hernan.vargas@utp.edu.co, aaog@utp.edu.co
[b] *Signal Processing and Recognition Group, Universidad Nacional de Colombia sede Manizales, Km 7 Via al Magdalena, Manizales, Colombia, 170001,*
E-mail: amalvarezme@unal.edu.co
[c] *Department of Computer Science, University of Sheffield, 211 Portobello , Sheffield, UK,*
E-mail: mauricio.alvarez@sheffield.ac.uk

Abstract

Diffusion magnetic resonance imaging (dMRI) is an established medical technique used for describing water diffusion in an organic tissue. Typically, rank-2 or 2nd-order tensors quantify this diffusion. From this quantification, it is possible to calculate relevant scalar measures (i.e. fractional anisotropy) employed in the clinical diagnosis of neurological diseases. Nonetheless, 2nd-order tensors fail to represent complex tissue structures like crossing fibers. To overcome this limitation, several researchers proposed a diffusion representation with higher order tensors (HOT), specifically 4th and 6th orders. However, the current acquisition protocols of dMRI data allow images with a spatial resolution between 1 mm^3 and 2 mm^3, and this voxel size is much bigger than tissue structures. Therefore, several clinical procedures derived from dMRI may be inaccurate. Concerning this, interpolation has been used to enhance the resolution of dMRI in a tensorial space. Most interpolation methods are valid only for rank-2 tensors and a generalization for HOT data is missing. In this work, we propose a

Email addresses: hernan.vargas@utp.edu.co (Hernán Darío Vargas-Cardona*[a]), aaog@utp.edu.co (Álvaro A. Orozco[a]), andres.alvarez1@utp.edu.co (Andrés M. Álvarez[b]), mauricio.alvarez@sheffield.ac.uk (Mauricio A. Álvarez[c])

[1]* Corresponding author.

probabilistic framework for performing HOT data interpolation. In particular, we introduce two novel probabilistic models based on the Tucker and the canonical decompositions. We call our approaches: Tucker decomposition process (TDP) and canonical decomposition process (CDP). We test the TDP and CDP in rank-2, 4 and 6 HOT fields. For rank-2 tensors, we compare against direct interpolation, log-Euclidean approach, and Generalized Wishart processes. For rank-4 and 6 tensors, we compare against direct interpolation and raw dMRI interpolation. Results obtained show that TDP and CDP interpolate accurately the HOT fields in terms of Frobenius distance, anisotropy measurements, and fiber tracts. Besides, CDP and TDP can be generalized to any rank. Also, the proposed framework keeps the mandatory constraint of positive definite tensors, and preserves morphological properties such as fractional anisotropy (FA), generalized anisotropy (GA) and tractography.

Keywords: Diffusion magnetic resonance imaging, higher order tensors, interpolation, probabilistic models, tensor decomposition.

---

1. Introduction

Diffusion magnetic resonance imaging (dMRI) is an established medical technique that non-invasively measures water diffusion in organic tissue. The first attempt to represent this physical phenomenon was the Gaussian model proposed by Basser et al. (1994, 1993), where symmetric and positive definite tensors of rank-2 are estimated from dMRI to quantify the direction and orientation of diffusion. This model is known as diffusion tensor imaging (DTI). From this quantification, it is possible to compute relevant physiological information (i.e. Fractional anisotropy and mean diffusivity) employed in the assessment of neurological diseases: Parkinson's disease (Butson et al., 2007), trauma (Ptak et al., 2003), multiple sclerosis (Hasan et al., 2005), meningitis (Nath et al., 2007), among others. Nevertheless, rank-2 tensors fail to represent accurately some complex tissue structures such as: white matter fiber bundles, crossing fibers, and bifurcated fibers (Mori et al., 1999; Ozarslan & Mareci, 2003).

To address these limitations in dMRI, several researchers have proposed higher order tensor (HOT) models for describing diffusion inside complex tissue structures (Barmpoutis & Vemuri, 2010; Liu et al., 2004; Moakher, 2008; Ozarslan & Mareci, 2003). These models demonstrated accuracy and flexibility to represent dMRI with low signal to noise ratio. However, the estimation of HOT requires more gradient directions for each slice in dMRI than the ones needed for DTI (Berman et al., 2013). Additionally, the current acquisition protocols of dMRI restrict the images to a voxel size in a range from 1 mm^3 to 2 mm^3, no matter if the representation is with HOT or DTI. The problem here is that this voxel size is much bigger than tissue fibers and current acquired dMRI of the human brain have a broad resolution in comparison to anatomical structures. Therefore, the analysis of microstructural features can be difficult and some clinical procedures derived from dMRI may be inaccurate (Dirby et al., 2014).

Interpolation of tensor fields is a feasible methodology to reduce the voxel size in dMRI and achieves clinical relevance in reconstruction of tissue fiber bundles for tractography. Furthermore, interpolation of tensor fields is important in any application where estimating data among nearby tensors is required, including image registration (Yassine & McGraw, 2009). A considerable number of methods for tensorial interpolation have been proposed in the literature, including direct linear interpolation (Pajevic et al., 2002), log-Euclidean space (Arsigny et al., 2006), b-splines (Barmpoutis et al., 2007), Riemannian manifolds (Fletcher & Joshi, 2007; Pennec et al., 2006), feature-based framework (Yang et al., 2012), geodesic loxodromes (Kindlmann et al., 2007) and generalized Wishart processes (Vargas Cardona et al., 2015). They have different shortcomings. For example, linear interpolation does not ensure positive definite tensors (Pajevic et al., 2002), and the works of Arsigny et al. (2006); Fletcher & Joshi (2007); Pennec et al. (2006) are highly affected by the intrinsic Rician noise added in dMRI during acquisition. Remarkably, the most significant limitation for all the approaches mentioned is that they are exclusively valid for rank-2 tensors (DTI), and only the linear interpolation can easily be employed on HOT fields. As we pointed out before, DTI is deficient to represent complex tissue structures. For this reason,

it is necessary a tensorial interpolation methodology that can be generalized to any order. The aim is to achieve a more accurate representation of the brain tissue.

Regarding HOT field interpolation, the authors of Yassine & McGraw (2008, 2009) developed a method based on tensor subdivision and minimization of two properties (curl and divergence) of the field for interpolation of 4th-order tensors. However, the works in Yassine & McGraw (2008, 2009) only reported outcomes for rank-4 tensor fields, and the methods do not have a clear extension to higher orders, lacking generalization. Another valid approach is to interpolate the dMRI before the tensor reconstruction. For example, in Dirby et al. (2014), it was demonstrated that interpolation of raw dMRI with conventional methods (linear, bicubic and b-spline) can reveal anatomical details only seen in very high resolution images. Though, this framework may produce the undesirable swelling effect in tensors (Yang et al., 2014) and blurs the tract boundaries (Dirby et al., 2014). Also, authors in Astola et al. (2011); Astola & Florack (2009) introduced an approach to perform probabilistic tractography in HOT data. In particular, they developed a Finsler geometry-based methodology for multi-fiber analysis. The Finsler geometry model is able to perform probabilistic tractography in HOT fields using the orientation distribution function (ODF), and it is a generalization of the streamline method applied on DTI (Astola et al., 2011). Nevertheless, a derived method of Finsler geometry for interpolation has not been developed yet.

To the best of our knowledge, there is not a generalized methodology for interpolating HOT fields (no matter the rank), that retains all mandatory constraints for tensorial representation of dMRI. In this work, we propose a novel methodology to perform interpolation in HOT fields of any order. In this regard, we employ tensor representations and modulate their parameters with Gaussian processes (GPs), aiming to estimate new data with robustness, considering that GPs are functions of a multi-dimensional input variable. Specifically, we introduce two probabilistic models, that we refer to as the Tucker decomposition process (TDP) and the canonical decomposition process (CDP). Our models

are based on the Tucker and canonical decomposition of tensors (Carroll & Chang, 1970; Gulliksen & Frederiksen, 1964), respectively. The main advantage of tensor decompositions is the transformation of a complex mathematical object in a superposition of scalars, vectors or matrices. These simple representations allow to index a tensor in an independent variable (i.e. spatial coordinates), facilitating the probabilistic modeling of tensor fields, no matter the order (rank). We test the TDP and CDP in 2nd, 4th and 6th rank HOT fields. For rank-2 tensors, we compare against direct interpolation (Pajevic et al., 2002), log-Euclidean approach (Arsigny et al., 2006), and Generalized Wishart processes (Vargas Cardona et al., 2015). For rank-4 and rank-6 tensors we compare against direct interpolation and raw dMRI interpolation with b-splines (Dirby et al., 2014). Results obtained show that TDP and CDP interpolate accurately the HOT fields, and generalize to any rank. Importantly, the proposed framework safeguards the mandatory constraint of positive definite tensors, and preserve morphological properties such as fractional anisotropy (FA), white matter (WM) segmentation, generalized anisotropy (GA), and tractography.

2. Materials and Methods

In this section, we first define the proposed framework. Second, we briefly explain the main concepts of a Gaussian process. Then, we introduce the Tucker and canonical decomposition of a tensor, and we describe the priors that we use to represent tensorial fields by combining the Tucker and canonical decomposition with Gaussian processes. Also, we introduce the higher order tensors for modeling dMRI data. Bayesian inference for the proposed probabilistic models is then discussed. Finally, we give details of the experimental setup.

2.1. Proposed approach for tensor interpolation

A tensor is a geometric or physical object specified by a set of coefficients $\mathcal{T}_{i_1 i_2 \ldots i_l}$ of a multi-linear form $\mathcal{T} = \phi(\mathbf{x}_1, \mathbf{x}_2, ..., \mathbf{x}_l) \in \mathbb{K}^{I_1 \times I_2 \times \ldots \times I_l}$ of l vector arguments $\mathbf{x}_1, \mathbf{x}_2, ..., \mathbf{x}_l$ written in some orthonormal basis, where $\mathbb{K}$ may refer to

$\mathbb{R}$ (real) or $\mathbb{C}$ (complex). The number l is known as the order or rank of the tensor and each vector argument has an independent (may be different) dimensionality. Alternatively, a tensor can be represented in several forms employing vectorial or matrix approximations:

$$\mathcal{T} \sim \mathbf{M}\left(\boldsymbol{\alpha}_1, \boldsymbol{\alpha}_2, ..., \boldsymbol{\alpha}_m\right),$$

being $\mathbf{M} \in \mathbb{K}^{I_1 \times I_2 \times ... \times I_l}$ any vectorial or matrix decomposition of $\mathcal{T}$, and $\boldsymbol{\alpha}_1, \boldsymbol{\alpha}_2, ..., \boldsymbol{\alpha}_m$ parameters of the given representation. Following this notion, our main goal is to develop probabilistic models (PM) over tensors indexed by an independent variable $\mathbf{z} = [z_1, z_2, ..., z_J]^\top$, being J the dimensionality of $\mathbf{z}$. For example, if $\mathbf{z}$ refers to spatial coordinates, then, $\mathbf{z} = [x, y, z]^\top$ and $J = 3$. The PM can be seen as probability distributions over a tensor field, this is, a grid of interconnected and related tensors. Furthermore, such probability distributions allow the interpolation of new tensor data for any input locations ($\mathbf{z}_*$), according to the following definition:

$$\mathcal{T}(\mathbf{z}) \sim \mathcal{M}\left(\boldsymbol{\alpha}_1(\mathbf{z}), \boldsymbol{\alpha}_2(\mathbf{z}), ..., \boldsymbol{\alpha}_m(\mathbf{z})\right), \tag{1}$$

where $\mathcal{M}$ is a tensor representation, and $\boldsymbol{\alpha}_1(\mathbf{z}), \boldsymbol{\alpha}_2(\mathbf{z}), ..., \boldsymbol{\alpha}_m(\mathbf{z})$ are free parameters that depend on the mathematical definition of $\mathcal{M}$. The probabilistic nature of $\mathcal{M}$ arises because the parameters $\boldsymbol{\alpha}_1(\mathbf{z}), \boldsymbol{\alpha}_2(\mathbf{z}), ..., \boldsymbol{\alpha}_m(\mathbf{z})$ are realizations of stochastic processes. Specifically to define $\mathcal{M}$, we employ the canonical (Carroll & Chang, 1970) and the Tucker decomposition (Gulliksen & Frederiksen, 1964) of tensors to construct the probabilistic model. The motivation of using both tensorial decompositions is for the simplicity in their representations. It is not necessary to model a complex object such a tensor, but simpler mathematical arrays: scalars, vectors and matrices. This allows to model a tensor field through stochastic methods (i.e. Gaussian processes) that modulate those scalars, vectors and matrices as function of an independent variable $\mathbf{z}$.

2.2. Gaussian process

A Gaussian Process (GP) is a collection of random variables which have a joint Gaussian distribution (Rasmussen & Williams, 2006). The GP can be understood as the generalization of a Gaussian distribution over a finite vector space to a function space of infinite dimension (Mackay, 1998). A GP is completely defined by its mean function, $\mu(\mathbf{z})$, and covariance function, $k(\mathbf{z}, \mathbf{z}')$, such that $f(\mathbf{z}) \sim \mathcal{GP}\left(\mu(\mathbf{z}), k(\mathbf{z}, \mathbf{z}')\right)$. For simplicity, the mean $\mu(\mathbf{z})$ is usually set to 0. In supervised learning, the squared exponential kernel is commonly employed as covariance function, and it is given by (Alvarez & Lawrence, 2011):

$$k(\mathbf{z}, \mathbf{z}') = \sigma_k^2 \exp\left(-\frac{||\mathbf{z} - \mathbf{z}'||^2}{2\theta^2}\right), \tag{2}$$

where θ and σ_k^2 are the length-scale and the variance hyperparameters, respectively.

2.3. Canonical decomposition of a tensor

Any tensor can always be decomposed (possibly non-uniquely) as:

$$\mathcal{T} = \sum_{i=1}^{r} \lambda_i \mathbf{u}_i \otimes \mathbf{v}_i \otimes \cdots \otimes \mathbf{w}_i, \tag{3}$$

where $\mathbf{u}_i \in \mathbb{R}^{I_1}$, $\mathbf{v}_i \in \mathbb{R}^{I_2}$, ... $\mathbf{w}_i \in \mathbb{R}^{I_l}$ are unitary vectors, $\lambda_i \in \mathbb{R}^+$ are generalized eigenvalues, and $\otimes$ denotes the outer or Kronecker product. The tensor rank, $\text{rank}(\mathcal{T})$, is the smallest integer r such that this decomposition holds exactly. The rank of $\mathcal{T} = [t_{j_1 \ldots j_l}] \in \mathbb{K}^{I_1 \times \ldots \times I_l}$ is defined as:

$$\text{rank}(\mathcal{T}) := \min\left\{ r \middle| \mathcal{T} = \sum_{i=1}^{r} \lambda_i \mathbf{u}_i \otimes \mathbf{v}_i \otimes \cdots \otimes \mathbf{w}_i \right\}.$$

If in (3), we have $\mathbf{u}_i = \mathbf{v}_i = \cdots = \mathbf{w}_i$ for every i, then we call it a symmetric outer product decomposition, yielding $I_1 = I_2 = I_l = n$, (being n the dimension of the tensor) and a symmetric rank, $\text{rank}_s(\mathcal{T})$:

$$\text{rank}_s(\mathcal{T}) := \min\left\{ s \middle| \mathcal{T} = \sum_{i=1}^{s} \lambda_i \mathbf{y}_i \otimes \cdots \otimes \mathbf{y}_i, \right\},$$

where $\mathbf{y}_i \in \mathbb{R}^n$ are unitary vectors. Henceforth, we will adopt the following notation:

$$\mathbf{y}^{\otimes l} = \mathbf{y} \otimes \cdots \otimes \mathbf{y},\ l \text{ copies}. \tag{4}$$

In addition to complete symmetry, some applications demand additional constraints, such as positivity definite tensors. Regarding this, a tensor $\mathcal{T}$ of even order is positive definite if and only if the smallest generalized eigenvalue $\lambda_{\min}$ of $\mathcal{T}$ is positive (Qi et al., 2009). The definition of symmetric rank is relevant because of the following proposition (Comon et al., 2008):

- *Let* $\mathcal{T} \in \mathbb{K}^{n \times \cdots \times n}$. *Then there exist* $\mathbf{y}_1, ..., \mathbf{y}_s \in \mathbb{K}^n$, *such that*

$$\mathcal{T} = \sum_{i=1}^{s} \lambda_i \mathbf{y}_i^{\otimes l}. \tag{5}$$

The above proposition establishes that a symmetric and positive definite tensor can be represented as the superposition of outer (Kronecker) products of s unitary vectors $\mathbf{y}_i \in \mathbb{K}^n$ scaled by the positive generalized eigenvalues $\lambda_i \in \mathbb{R}^+$, $i = 1, ..., s$. The outer product decomposition has often been regarded synonymously as the data analytic models CANDECOMP (Carroll & Chang, 1970) and PARAFAC (Harshman, 1970), where the decomposition is used to analyze multi-way psychometric data.

2.4. Canonical decomposition process (CDP)

The CANDECOMP is a superposition of outer products of scaled-vectors. This decomposition represents a symmetric tensor in s positive scalars λ_i and s unitary vectors $\mathbf{y}_i$ whose number of elements depends of the tensor dimensionality. The main advantage of the canonical decomposition is due to the easy reconstruction of the tensor, as we can see in equation (5). Also, it is worth noting the parameters of this decomposition are simple objects: scalars and vectors, that can easily be described through independent Gaussian processes.

According to the formulation given in equations (1) and (5), we propose a stochastic approach for tensorial interpolation. Let us define $\boldsymbol{\lambda}(\mathbf{z}) = \{\lambda_1, ..., \lambda_s\}$

as the eigenvalues vector. Following our general approach, the idea would be to index each λ_i by the spatial variable $\mathbf{z}$. Since the values of $\boldsymbol{\lambda}$ should remain positive, we transform the elements λ_i with a log function. Then, we assume that $\log(\lambda_i)$ follows a Gaussian process. Once we obtain the posterior of $\log \boldsymbol{\lambda}$, we apply the exp function to recover $\boldsymbol{\lambda}$. Also, for the entries in the unitary vectors $\mathbf{y}_i$ $(i = 1, ..., s)$, we assume each element y_{ij}, $(j = 1, ..., n)$ follows an independent Gaussian process. We normalize each $\mathbf{y}_i$ for ensuring unitary vectors. We refer to this process by the name of the *canonical decomposition process (CDP)*:

$$\mathcal{T}(\mathbf{z}) \sim \mathcal{CDP}(\boldsymbol{\lambda}(\mathbf{z}), \mathbf{y}_i(\mathbf{z}), s, l) = \sum_{i=1}^{s} \lambda_i(\mathbf{z}) \mathbf{y}_i(\mathbf{z})^{\otimes l}, \tag{6}$$

where, $\log \lambda_i(\mathbf{z}) \sim \mathcal{GP}(\mu, k(\mathbf{z}, \mathbf{z}'))$ and $y_{ji}(\mathbf{z}) \sim \mathcal{GP}(0, k(\mathbf{z}, \mathbf{z}'))$. We use an squared exponential kernel (see equation (2)), for constructing the covariance of the GPs (Rasmussen & Williams, 2006).

2.5. Tucker decomposition of a Tensor

Consider $\mathcal{T} \in \mathbb{K}^{I_1 \times I_2 \ldots \times I_l}$ and $\mathbf{A}^{(1)} \in \mathbb{K}^{J_1 \times I_1}$, $\mathbf{A}^{(2)} \in \mathbb{K}^{J_2 \times I_2}$ and $\mathbf{A}^{(l)} \in \mathbb{K}^{J_l \times I_l}$. Then, the Tucker mode-1 product $\mathcal{T} \cdot_1 \mathbf{A}^{(1)}$, mode-2 product $\mathcal{T} \cdot_2 \mathbf{A}^{(2)}$ and mode-l product $\mathcal{T} \cdot_l \mathbf{A}^{(l)}$ are defined by

$$\left(\mathcal{T} \cdot_1 \mathbf{A}^{(1)}\right)_{j_1 i_2 \ldots i_l} = \sum_{i_1=1}^{I_1} \mathcal{T}_{i_1 i_2 \ldots i_l} A^{(1)}_{j_1 i_1}, \ \forall j_1, i_2, ..., i_l,$$

$$\left(\mathcal{T} \cdot_2 \mathbf{A}^{(2)}\right)_{i_1 j_2 \ldots i_l} = \sum_{i_2=1}^{I_2} \mathcal{T}_{i_1 i_2 \ldots i_l} A^{(2)}_{j_2 i_2}, \ \forall i_1, j_2, ..., i_l,$$

$$\left(\mathcal{T} \cdot_l \mathbf{A}^{(l)}\right)_{i_1 i_2 \ldots j_l} = \sum_{i_l=1}^{I_l} \mathcal{T}_{i_1 i_2 \ldots i_l} A^{(l)}_{j_l i_l}, \ \forall i_1, i_2, ..., j_l.$$

A Tucker decomposition of a cubic tensor ($I_1 = I_2 = I_l = n$) $\mathcal{T} \in \mathbb{K}^{n \times \ldots \times n}$ is a decomposition of $\mathcal{T}$ of the form (Gulliksen & Frederiksen, 1964):

$$\mathcal{T} = \mathcal{C} \cdot_1 \mathbf{A}^{(1)} \cdot_2 \cdots \mathbf{A}^{(l-1)} \cdot_l \mathbf{A}^{(l)}, \tag{7}$$

for which $\mathcal{C} \in \mathbb{K}^{n \times \ldots \times n}$ is known as the core tensor, and $\mathbf{A}^{(1)}$, $\mathbf{A}^{(2)}$,..., $\mathbf{A}^{(l)} \in \mathbb{K}^{n \times R}$ $(R \leq n)$ are matrices with column unitary vectors. If the decomposed

tensor is symmetric and positive definite, $\mathbf{A}^{(1)} = \mathbf{A}^{(2)} = ... = \mathbf{A}^{(l)}$. For an $l-$order tensor, equation (7) is rewritten as follows:

$$\mathcal{T} = \mathcal{C} \cdot_1 \mathbf{A} \cdot_2 \cdots \mathbf{A} \cdot_l \mathbf{A} = \left[\mathbf{A} \otimes^l \mathbf{A}\right] \operatorname{vec} \mathcal{C}, \tag{8}$$

where vec is an operator that transforms a tensor into a vector.

2.6. Tucker Decomposition Process (TDP)

The Tucker decomposition is defined by a set of outer products of matrices multiplied by a core tensor. The advantage of Tucker is that it guarantees an exact decomposition, while CANDECOMP may be approximated in some cases. Also, when the tensor is symmetric, the size of representation matrix $\mathbf{A}$ does not depend of the rank, which is a remarkable aspect, because higher orders fields do not increase considerably the time necessary for executing the learning stage.

Based on equations (1) and (8), we propose an additional model for tensorial interpolation that we call *Tucker decomposition process* (TDP). Let $\mathcal{T}(\mathbf{z})$ be a random field of tensors. We say that $\mathcal{T}(\mathbf{z})$ follows a TDP according to:

$$\mathcal{T}(\mathbf{z}) \sim \mathcal{TDP}(\mathcal{C}, \mathbf{A}(\mathbf{z}), l) = \mathcal{C} \cdot_1 \mathbf{A}(\mathbf{z}) \cdot_2 \cdots \mathbf{A}(\mathbf{z}) \cdot_l \mathbf{A}(\mathbf{z}) = \left[\mathbf{A}(\mathbf{z}) \otimes^l \mathbf{A}(\mathbf{z})\right] \operatorname{vec} \mathcal{C}, \tag{9}$$

where $\mathcal{C}$ is a $l-$order symmetric core tensor, and $\mathbf{A}$ is a $n \times R$ matrix with column unitary vectors. The variable n is the tensorial dimension, and R is the degree of the decomposition ($R \leq n$). In our probabilistic model, we assume that each element of $\mathbf{A}$ follows an independent GP indexed by $\mathbf{z}$. Again, we normalize each column vector of $\mathbf{A}$ for ensuring unitary vectors. Also, we establish that the unique elements of the core tensor $\mathcal{C}$ are random variables sampled from a spherical multivariate Gaussian distribution. The number of unique elements of a tensor depends on its order l. For example if $l = 4$, we have $E_l = 15$ unique elements in a 4_{th} order tensor. The prior distributions over the parameters in the *TDP* are given by $\mathbf{A}(\mathbf{z})$ with elements $A_{ij}(\mathbf{z}) \sim \mathcal{GP}(0, k(\mathbf{z}, \mathbf{z}'))$ for $i, j = 1, 2, 3$; $\operatorname{vec} \mathcal{C} \sim \mathcal{N}(\mathbf{0}, c^2\mathbf{I})$, with c^2 the common variance for the elements in $\operatorname{vec} \mathcal{C}$.

2.7. Higher Order Tensors and dMRI

In previous subsections, we introduced two probabilistic models (CDP and TDP) for describing tensor fields of any order indexed by an independent variable (i.e. spatial coordinates). In the context of diffusion magnetic resonance imaging (dMRI), higher order tensors (HOT) are employed for modeling diffusion of water particles in organic tissue. A HOT $\in \mathbb{R}^{n_1 \times \ldots \times n_l}$ has a dimensionality $n = 3$ for all array arguments, $n_1 = n_2 = ... = n_l = 3$. A structured diffusion process through dMRI is defined by the generalized Stejskal-Tanner formula (Ozarslan & Mareci, 2003):

$$\log S_k(\mathbf{z}) = \log S_0(\mathbf{z}) - b \times \sum_{i_1=1}^{3} \sum_{i_2=1}^{3} \cdots \sum_{i_l=1}^{3} \mathcal{D}^{(l)}_{i_1 i_2 \ldots i_l}(\mathbf{z}) g_{i_1} g_{i_2} \cdots g_{i_l}, \qquad (10)$$

where S_k is the k_{th} dMRI acquired in a particular input position $\mathbf{z} = [x, y, z]^\top$, S_0 is the baseline image, b is the diffusion coefficient, l is the order of tensor, $g_{i_1} g_{i_2} \cdots g_{i_l}$ is the direction of a gradient vector, and $\mathcal{D}_{i_1 i_2 \ldots i_l}$ is the diffusion tensor. From equation (10), it is possible to compute all elements of a tensor using multi-linear regression (Barmpoutis & Vemuri, 2010), for all input locations in a dMRI. The diffusion function $\mathcal{D}(g)$ is defined as:

$$\mathcal{D}(g) = \sum_{i_1=1}^{3} \sum_{i_2=1}^{3} \cdots \sum_{i_l=1}^{3} \mathcal{D}_{i_1 i_2 \ldots i_l} g_{i_1 i_2 \ldots i_l}.$$

The order l must be strictly even: an odd l implies that $\mathcal{D}(-g) = -\mathcal{D}(g)$, leading to non-positive definite tensors, that do not have physical interpretation. For this reason, the rank of a higher order tensor (HOT) always must be even. A rank-l tensor has 3^l elements. This number is very large for higher orders. But total symmetry of HOT reduces significantly the number of unique components of the tensor to $E_l = \frac{(l+1)(l+2)}{2}$.

From a whole dMRI study, it is possible to estimate a tensor field. A HOT has a discrete graphical representation defined by parametrized surfaces known as glyphs (Ozarslan & Mareci, 2003). Figure 1 shows examples of HOT fields of rank-2,4 and 6.

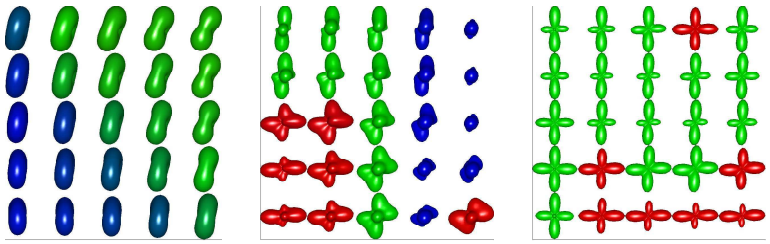

(a) (b) (c)

Figure 1: Examples of HOT fields: (a) rank-2, (b) rank-4, and (c) rank-6. RGB colors indicate the principal direction of the diffusion tensor: right-left (RED), anterior-posterior (GREEN) and ventral-inferior (BLUE)

2.8. Bayesian inference for TDP and CDP

For TDP and CDP, we follow the classical Bayesian approach for finding the posterior parameters:

$$\textit{posterior} \propto \textit{prior} \times \textit{likelihood}.$$

Given a finite set of higher order tensors $\mathcal{X}(\mathbf{Z}) = \{\mathcal{D}(\mathbf{z}_i)\}_{i=1}^{N}$, obtained from solving the Stejskal-Tanner formula for different input locations $\mathbf{z}_i$ ($\mathbf{Z} \in \mathbb{R}^{n \times N}$ is a matrix that contains all spatial locations of the training set, and N is the number of training data), we use Bayesian inference to compute the posterior distribution for the HOT field:

$$p(\mathcal{T}(\mathbf{z})|\mathcal{X}(\mathbf{Z})) \propto p(\mathcal{T}(\mathbf{z}))p(\mathcal{X}(\mathbf{Z})|\mathcal{T}(\mathbf{z})).$$

We use the TDP or the CDP as the prior for $p(\mathcal{T}(\mathbf{z}))$, and for the likelihood function, we assume each element from the HOT data follows an independent Gaussian distribution with the same variance σ^2. This leads to a likelihood with the form:

$$p(\mathcal{X}(\mathbf{Z})|\mathcal{T}(\mathbf{z})) \propto \prod_{i=1}^{N} \exp\left(-\frac{1}{2\sigma^2}\|\mathcal{X}(\mathbf{z}_i) - \mathcal{T}(\mathbf{z}_i)\|_F^2\right),$$

where $\|\mathcal{A} - \mathcal{B}\|_F$ is the tensorial Frobenius distance of order l given by

$$\|\mathcal{A} - \mathcal{B}\|_F = \left(\sum_{i_1,\ldots,i_l}^{3} \left(\mathcal{A}_{i_1,\ldots,i_l} - \mathcal{B}_{i_1,\ldots,i_l}\right)^2\right)^{1/2}. \tag{11}$$

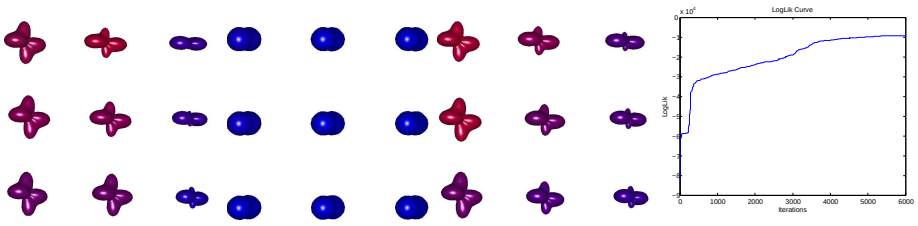

(a) Training data (b) Prior (c) Posterior (d) LogLik curve

Figure 2: Learning process for a 3×3 rank-4 HOT field. (a) is the training set (low spatial resolution field), (b) is the initial field obtained from the TDP prior, (c) is the posterior field obtained after 6000 iterations, and (d) is the learning curve given by the log-likelihood.

Posterior distributions for the TDP are computed for matrix $\mathbf{A}(\mathbf{z})$, the length-scale parameter θ of the squared exponential kernel (for which a log-normal prior is used), and the core tensor $\mathcal{C}$. We use Markov chain Monte Carlo algorithms to sample in cycles. The variance parameter σ_k^2 of the kernel is set to 1 for ensuring the restriction $k(\mathbf{z}, \mathbf{z}) = 1$. Metropolis-Hastings (Robert & Casella, 2005) is used to sample the posterior of θ, and for the elements of the core tensor $\mathcal{C}$. To sample $\mathbf{A}(\mathbf{z})$, we employ elliptical slice sampling (Murray et al., 2010). We set $R = n = 3$ no matter the rank of the HOT field. For the CDP, we employ elliptical slice sampling for obtaining the posterior of $\boldsymbol{\lambda}(\mathbf{z})$ and $\mathbf{y}_i(\mathbf{z})$. We set $s = 8$ when the rank $l = 2$, $s = 10$ when $l = 4$, and $s = 12$ when $l = 6$.

We obtain initial values of relevant parameters sampling from the priors. For MCMC methods, we employ 7000, 9000, 11000 cycles for rank-2, 4 and 6 respectively, adding 1300 for the burn-in stage. The goal of the burn-in is to guarantee statistical independence among samples. For Metropolis-Hastings algorithm, we employ a Gaussian function as proposal distribution with $\sigma^2 = 0.001$. For elliptical slice sampling, we set a different rate parameter (lr) depending of the rank. For rank-2 tensors we set $lr = 0.001$, for rank-4 and 6 we set $lr = 0.0001$. Coefficients of the tensors are scaled in the range -5 to 5. Figure 2 shows an example of the learning process for the TDP.

2.9. HOT prediction with the TDP and CDP

Once we learn the posterior distribution for all the parameters, we compute the predictive distribution for $p(\mathcal{T}(\mathbf{z}_*)|\mathcal{T}(\mathbf{z}), \mathbf{z}_*)$, in a new spatial position $\mathbf{z}_* = [x_*, y_*, z_*]^\top$.

First, we have to infer the distribution over all unknown GP function values from $\mathbf{A}(\mathbf{z}_*)$ for the TDP and $\boldsymbol{\lambda}(\mathbf{z}_*)$, $\mathbf{y}_i(\mathbf{z}_*)$ for the CDP. If we vectorized all elements of $\mathbf{A}(\mathbf{z})$, $\mathbf{A}(\mathbf{z}_*)$; $\boldsymbol{\lambda}(\mathbf{z})$, $\boldsymbol{\lambda}(\mathbf{z}_*)$, $\mathbf{y}_i(\mathbf{z})$, $\mathbf{y}_i(\mathbf{z}_*)$, we obtain two vectors $\mathbf{u}$ and $\mathbf{u}_*$ with $p = nRN$ and $q = nRN_v$ (for TDP) or $p = nsN$ and $q = nsN_v$ (for CDP) elements, respectively. N is the number of training data and N_v is the number of validation data. The joint distribution over $\mathbf{u}$ and $\mathbf{u}_*$ is given by,

$$\begin{bmatrix} \mathbf{u} \\ \mathbf{u}_* \end{bmatrix} \sim \mathcal{N}\left(\mathbf{0}, \begin{bmatrix} \mathbf{K_B} & \mathbf{B}^\top \\ \mathbf{B} & \mathbf{K}^* \end{bmatrix}\right).$$

Here, $\mathbf{K_B}$ is a $nRN \times nRN$ (TDP) or $nsN \times nsN$ (CDP) block diagonal covariance matrix, where each block is a $N \times N$ Gram matrix $\mathbf{K}$ with entries $K_{ij} = k(\mathbf{z}_i, \mathbf{z}_j)$, being $k(\cdot, \cdot)$ the squared exponential kernel. If $\mathbf{u}_*$ and $\mathbf{u}$ have p and q elements respectively, $\mathbf{B}$ is a $p \times q$ matrix that represents the covariances between $\mathbf{u}_*$ and $\mathbf{u}$ for all pairs of training and validation data, this is $B_{ij} = k_i(\mathbf{z}_*, \mathbf{z}_j)$ for $i + (i-1)N \leq j \leq iN$, and 0 otherwise. $\mathbf{K}^*$ is a $p \times p$ Gram matrix with entries $K^*_{ij} = k(\mathbf{z}_{*i}, \mathbf{z}_{*j})$, being $\mathbf{z}_*$, the spatial coordinates of the test data. Using the properties of a Gaussian distribution, and conditioning on $\mathbf{u}$, we obtain:

$$p\left(\mathbf{u}_*|\mathbf{u}\right) \sim \mathcal{N}\left(\mathbf{B}{\mathbf{K_B}}^{-1}\mathbf{u}, \mathbf{K}^* - \mathbf{B}{\mathbf{K_B}}^{-1}\mathbf{B}^\top\right). \tag{12}$$

From the mean value for $\mathbf{u}_*$ obtained from $p\left(\mathbf{u}_*|\mathbf{u}\right)$, we organize $\mathbf{A}(\mathbf{z}_*)$ or $\boldsymbol{\lambda}(\mathbf{z}_*)$ and $\mathbf{y}_i(\mathbf{z}_*)$. Then, we compute $\mathcal{T}(\mathbf{z}_*)$ using equations (6) and (9) for CDP and TDP, respectively.

2.10. Experimental setup and datasets

We test the TDP and CDP in HOT fields of rank 2,4 and 6 in two different types of datasets. First, we obtain a 2D synthetic crossing fibers field (30×30 vox-

els) from the algorithm of the fanDTasia toolbox (Barmpoutis & Vemuri, 2010), available at `http://www.cise.ufl.edu/~abarmpou/lab/fanDTasia/`. Second, we estimate HOT data from a real dMRI study using the method proposed in Barmpoutis & Vemuri (2010). The dMRI study was downloaded from the *human connectome project*: `https://www.humanconnectome.org/`, specifically from *MGH Adult Diffusion Data* repository. The data were collected from a male subject (age between 20-24) on the customized Siemens 3T Connectom scanner, a 64-channel tight-fitting brain array coil was used for data acquisition, and 70 gradient directions with a value for b equal to 5000 S/mm^2. The study contains $140 \times 140 \times 96$ images in the axial plane with isotropic voxel size of 1.5 mm, and we select a region of interest (ROI) of $40 \times 40 \times 10$ voxels centered in the corpus callosum. As ground-truth or gold standard we use the original HOT data (synthetic and real), then we downsample the HOT fields by a factor of two. The downsampled fields are the training sets. In this work, we split the entire field in four subfields in order to seek a faster execution of algorithms. We test the proposed methods simultaneously over each subfield. CDP and TDP are patch-based methods, then we select a 3×3 patch for the training, obtaining a 5×5 patch in the validation stage. The patch is moved across the subfield for processing all tensors.

After we train the TDP and CDP, we compute the predictive distribution for the HOT fields. For rank-2 data, we compare our approaches with direct linear interpolation (Pajevic et al., 2002), log-Euclidean interpolation (Arsigny et al., 2006), and generalized Wishart processes (GWP) (Vargas Cardona et al., 2015). For rank-4 and 6, we compare against direct linear interpolation and raw dMRI interpolation with b-splines (only for the real dMRI data set). For a quantitative evaluation, we calculate an error metric based on the tensorial Frobenius distance (see eq. (11)) between the interpolated field and the respective ground-truth, evaluating only the predicted tensors. Also, we test morphological validation employing fractional anisotropy (FA) maps and tractography analysis (2D and 3D) for rank-2 tensors. FA is a measurement of anisotropy levels in dMRI, where a 0 value corresponds to an isotropic tensor and 1 refers to a full

anisotropic tensor. In the case of 3D tractography, we evaluate the number of generated fibers and the average length of tracts. For rank-4 and 6, we evaluate generalized anisotropy (GA) curves. GA is a generalization of FA for higher orders. Additionally, we perform an experiment related to white matter segmentation over second order fields through thresholding of FA images and graph cuts Shi & Malik (2000). Finally, we measure the computational time for each method in a PC: Intel Core-i7, 3,4 GHz, 16 Gb RAM; and we perform a $\times 4$ interpolation for evaluating the generalization capability of methods when we have a few amount of training data. Figure 3 illustrates a flow diagram of the proposed framework.

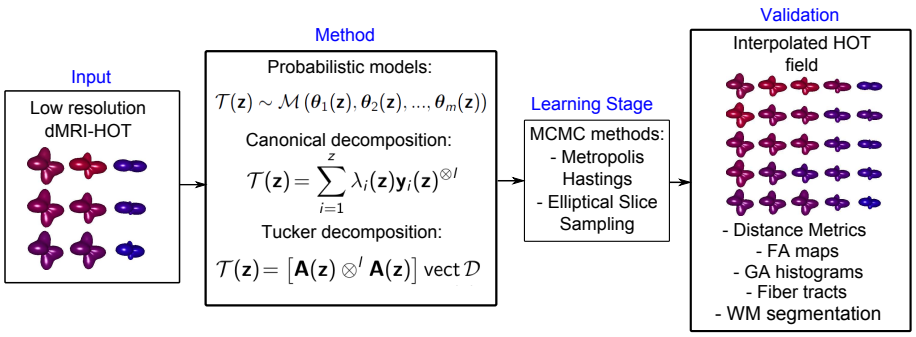

Figure 3: Flow diagram of the proposed framework. The input is a low resolution field (i.e. 3×3 tensors). Then, we model the HOT field with CDP or TDP. Next, we find the posterior of parameters employing MCMC methods. Finally, we validate the enhanced resolution field (i.e. 5×5 tensors) comparing with a gold standard through distance metrics, FA maps, GA histograms, fiber tracts, and white matter segmentation.

3. Results and Discussion

In this section, we first illustrate how parameters of the models are estimated using Monte Carlo methods. Second, we perform a Rician noise analysis evaluating error in interpolation of 2D synthetic tensor fields (30×30 voxels) for various signal-to-noise ratio (SNR) values. Then, we show quantitative and qualitative results obtained in two different dMRI data: a simulation of crossing fibers field

and a real dMRI study acquired from a human subject. For all datasets, we interpolate HOT fields of rank 2,4 and 6.

3.1. Monte Carlo methods

Figure 4 shows the samples and posterior distributions of relevant parameters for CDP and TDP, when we train a rank-2 synthetic field: length-scale (θ), y_{11} element of CDP and A_{11} element for TDP respectively. In this case, the initial values of mentioned parameters are sampled from the priors. Recall that the prior of θ is a log-normal distribution with $\mu_\theta = 0$ and $\sigma_\theta = 0.001$ while elements of vectors $\mathbf{y}_i$ and matrix $\mathbf{A}$ follow independent Gaussian processes $\mathcal{GP}(\mathbf{0}, k(\mathbf{z}, \mathbf{z}))$. A closer look to figure 4 demonstrates a stable behavior of all parameters analyzed. For example, the θ hyper-parameter has some strong jumps, but its distribution function is not highly disperse. y_{11} and A_{11} have a similar tendency, where they present an unique mode.

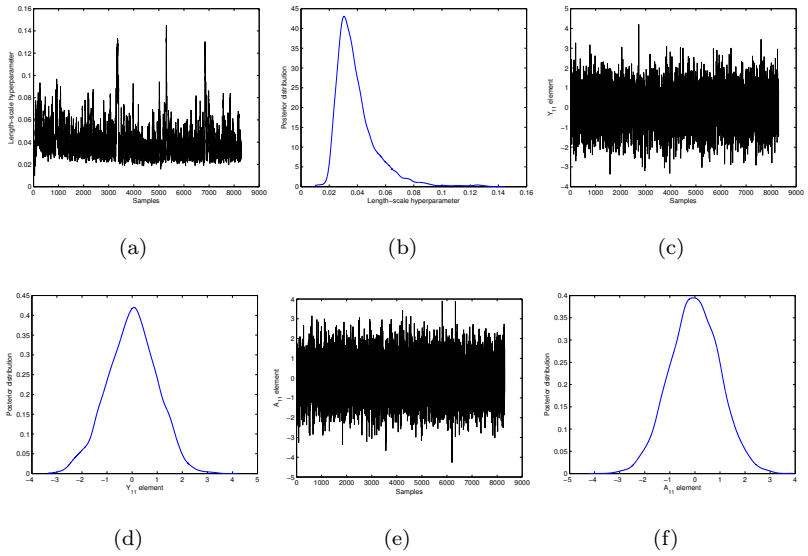

(a) (b) (c)

(d) (e) (f)

Figure 4: Samples and posterior distributions obtained for some relevant parameters: a) and b) correspond to the length-scale hyper-parameter θ of the squared exponential kernel $k(\mathbf{z}, \mathbf{z}')$; c) and d) illustrate the element y_{11} of the unitary vector $\mathbf{y}_1$ used in CDP; e) and f) refer to the element A_{11} of the matrix $\mathbf{A}$ employed in TDP. Metropolis-Hastings is used for θ, and elliptical slice sampling is the algorithm used for elements of $\mathbf{y}_i$ and $\mathbf{A}$.

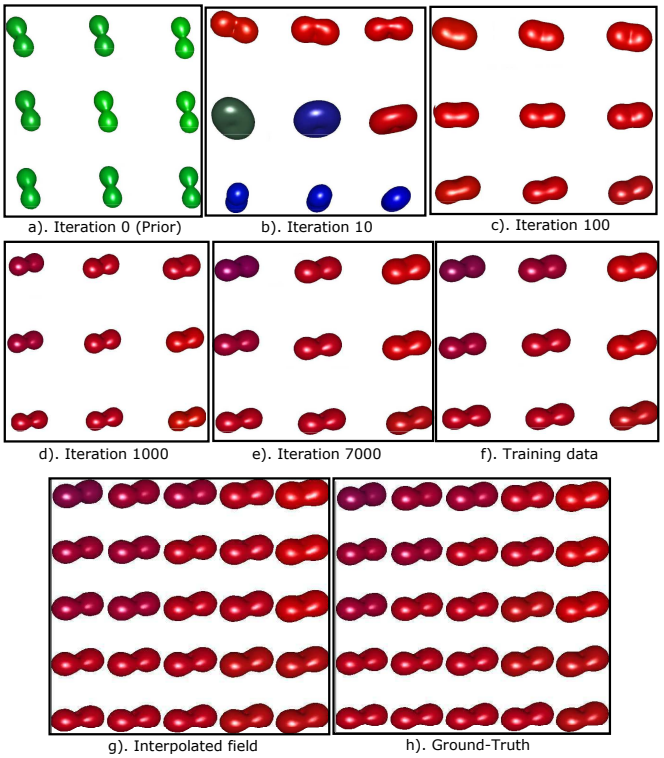

Figure 5: Learning and predictive process for a rank-2 synthetic field. Subfigures a) to e) show the evolution of a initial field obtained from sampling a prior (in this example we employ CDP, but a similar process occurs for TDP) until the learning stage is completed in iteration 7000 (recall, we employ 1300 samples in the burn-in stage); f) corresponds to the training data or low resolution field; g) corresponds to the interpolated or high resolution field, and h) is the ground-truth data.

Figure 5 describes the learning and prediction process for a rank-2 tensor field. As we can observe, the initial field obtained from the prior (CDP or TDP) is gradually modified until it achieves the values and shapes of the training data. To construct the posterior of CDP and TDP, we select the parameters with the biggest log-likelihood. Then, using the predictive distribution, we interpolate new data for enhancing spatial resolution of the tensor field.

3.2. Noise Analysis

We perform a noise analysis by testing the interpolation methods over tensor data corrupted with Rician noise for several SNR values. The noise is randomly distributed in the tensor field. Figures 6 and 8 show training data and ground truth for rank-2 and 4, respectively. Also, figures 7 and 9 show the mean error and standard deviation of interpolation in rank-2 and 4. For all magnitude variations of SNR and different tensor orders (including rank-6), the proposed methods outperform to the comparison approaches.

3.2.1. Rank-2 data

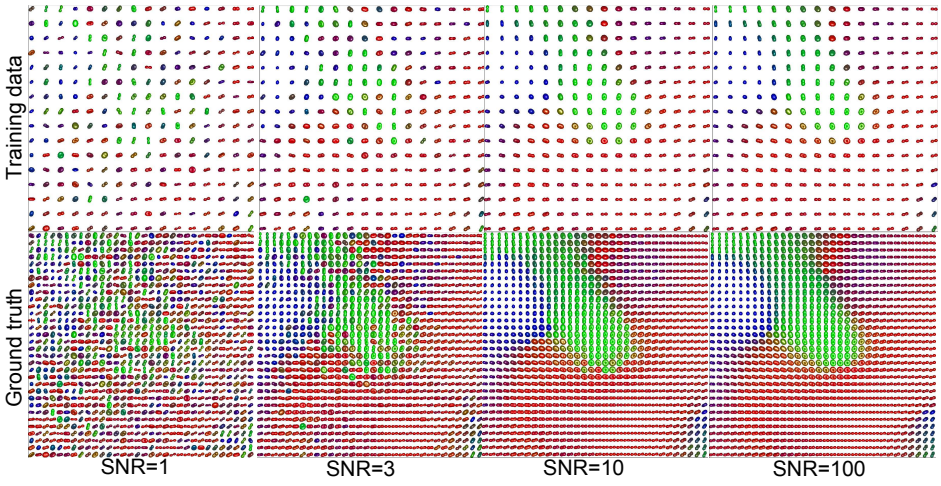

Figure 6: Rank-2 synthetic data corrupted with Rician noise for several SNR values. Top and bottom row correspond to the training data and ground truth respectively.

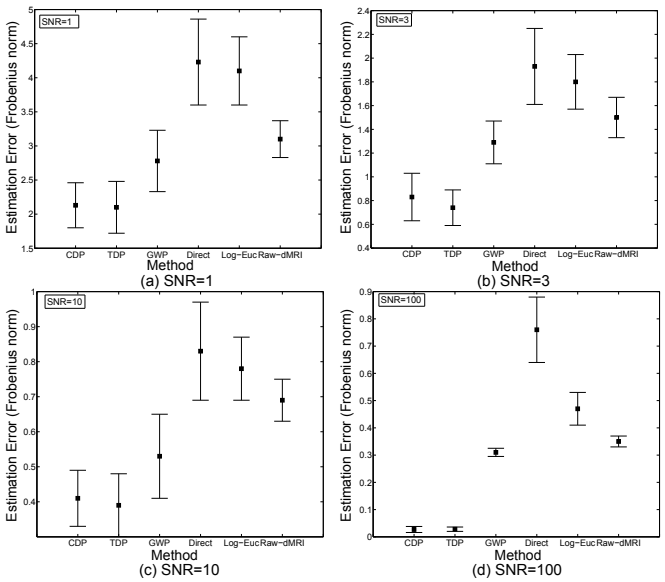

Figure 7: Mean and standard deviation of interpolation error (Frobenius norm) in rank-2 synthetic data for SNR equals to 1, 3, 10, and 100.

3.2.2. Rank-4 data

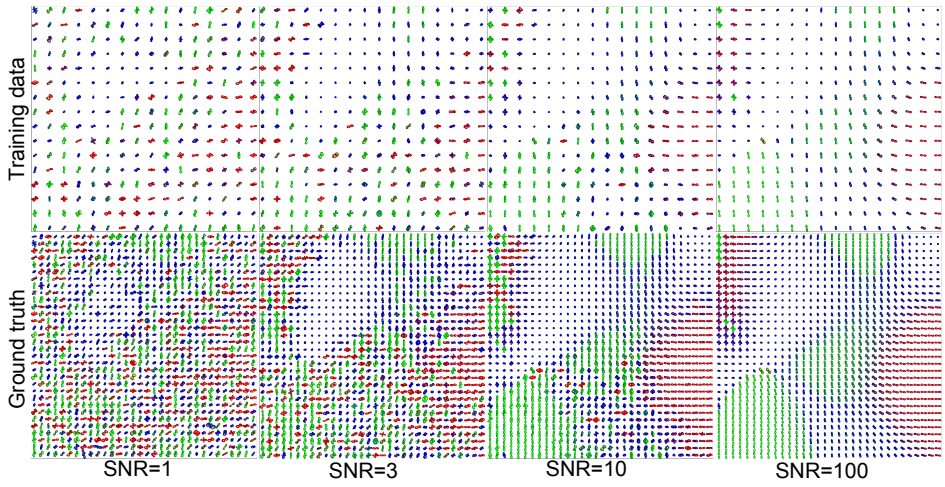

Figure 8: Rank-4 synthetic data corrupted with Rician noise for several SNR values.

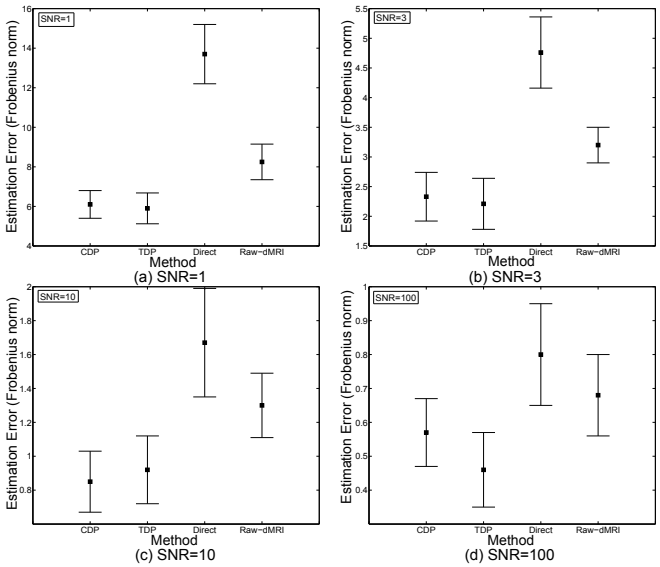

Figure 9: Mean and standard deviation of interpolation error in rank-4 synthetic data for several SNR values.

3.3. HOT fields interpolation in crossing fibers data

3.3.1. Rank-2 Results

Figure 10 and Table 1 show results for the rank-2 crossing fibers field. Again, CDP and TDP outperform direct interpolation, Generalized Wishart processes (GWP) and log-Euclidean interpolation, when we evaluate accuracy and morphological validation.

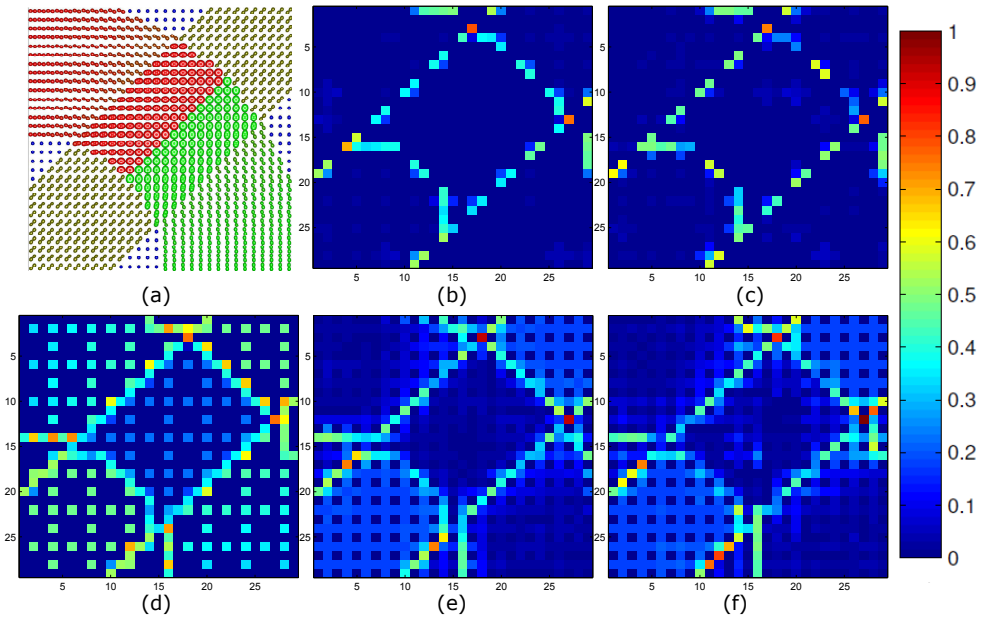

Figure 10: Normalized error maps for interpolation of a rank-2 crossing fibers HOT field: (a) Ground-truth, (b) CDP, (c) TDP, (d) Direct interpolation , (e) GWP, and (f) log-Euclidean.

Table 1: Frobenius distance and MSE of FA for rank-2 crossing fibers HOT field

	D. interpolation	Log-Euclidean	GWP	TDP	CDP
Frobenius distance (FD)	0.551 ± 0.625	0.505 ± 0.531	0.372 ± 0.353	0.139 ± 0.112	$\mathbf{0.125 \pm 0.110}$
MSE of FA ($\times 10^{-3}$)	9.62 ± 3.34	9.53 ± 3.38	4.60 ± 2.30	3.90 ± 2.25	$\mathbf{3.90 \pm 2.36}$
Interface (FD)	0.881 ± 0.223	0.798 ± 0.195	0.671 ± 0.147	0.551 ± 0.115	$\mathbf{0.521 \pm 0.121}$

3.3.2. Rank-4 and 6 results

Table 2: Frobenius distance for rank-4 and 6 crossing fibers HOT fields

	CDP	TDP	Direct interpolation
Rank-4	$\mathbf{0.734 \pm 0.634}$	0.790 ± 0.731	1.106 ± 1.957
Rank-6	$\mathbf{1.514 \pm 1.013}$	1.632 ± 0.994	2.276 ± 2.776
Interface (Rank-4)	$\mathbf{1.841 \pm 0.522}$	2.421 ± 0.501	2.954 ± 0.756
Interface (Rank-6)	$\mathbf{3.241 \pm 0.898}$	3.577 ± 0.847	3.624 ± 0.898

Table 2 shows the average Frobenius distance for HOT interpolation in rank-4 and 6 crossing fibers data. Figures 11 and 12 show the error map for rank-6 and the histogram of generalized anisotropy (GA) for rank-4, respectively.

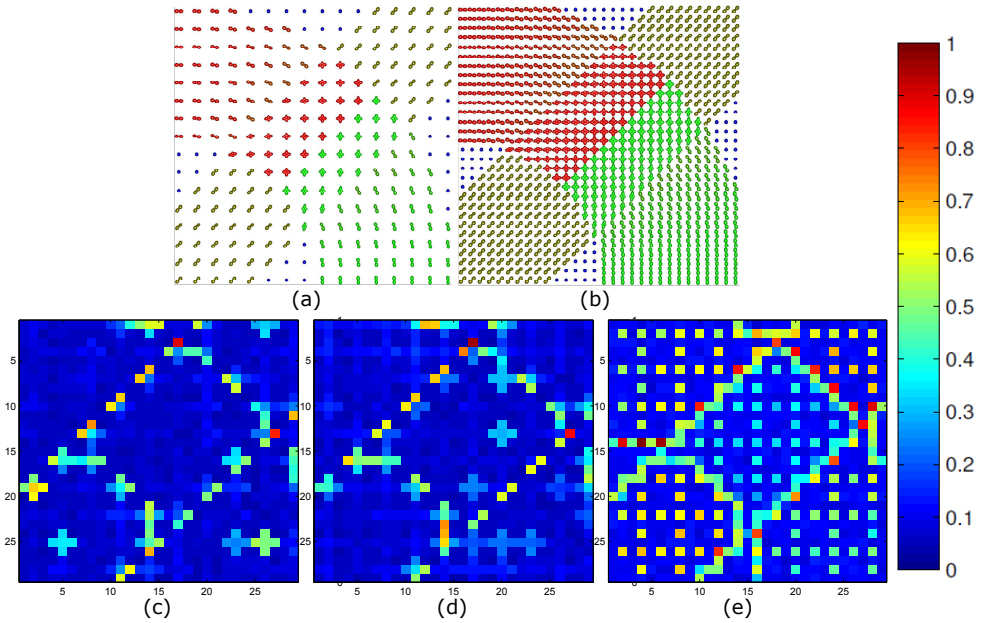

Figure 11: Normalized error maps (Frobenius distance) for interpolation of rank-6 crossing fibers HOT field: (a) Training data, (b) Ground-truth, (c) CDP, (d) TDP, (e) linear interpolation.

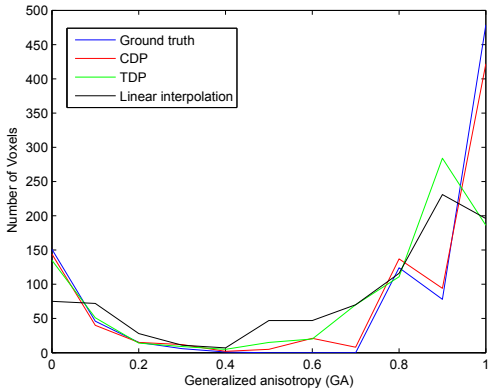

Figure 12: Generalized anisotropy (GA) curve for the rank-4 crossing fibers HOT field

3.4. HOT fields interpolation in real dMRI data

3.4.1. Rank-2 Results

Figure 13 and Table 3 show results for the rank-2 real data. Similar to the results for the synthetic and crossing fibers examples, the CDP and TDP offer better performance compared to the linear, log-Euclidean interpolation and GWP.

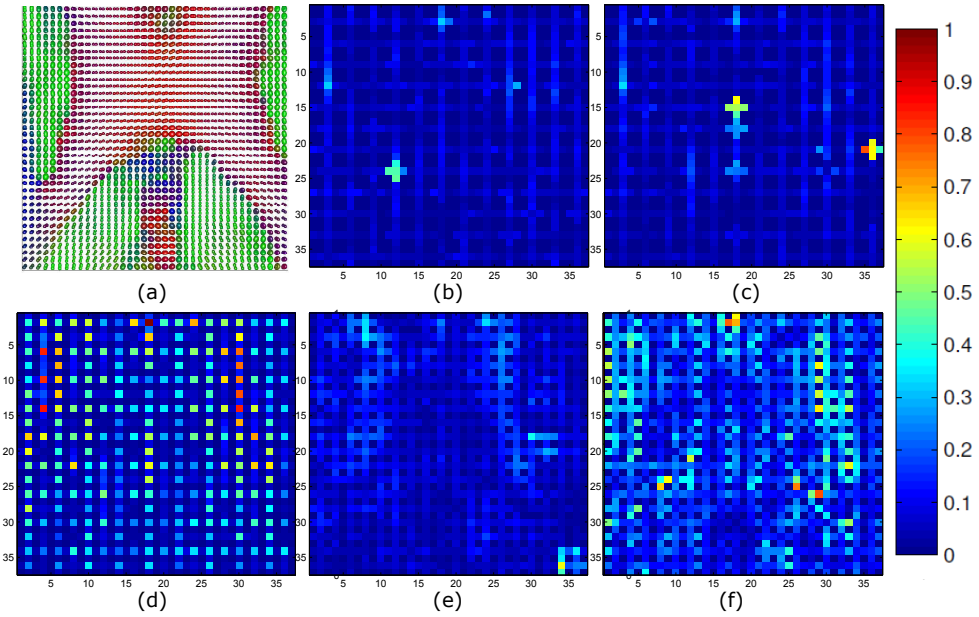

Figure 13: Normalized error maps for interpolation of rank-2 real HOT field: (a) Ground-truth data, (b) CDP, (c) TDP, (d) direct interpolation, (e) GWP, and (f) log-Euclidean. The analyzed region is a slice of the corpus callosum.

Table 3: Frobenius distance for rank-2 real HOT field

	Direct interpolation	Log-Euclidean	GWP	TDP	CDP
Frobenius distance	0.275 ± 0.219	0.224 ± 0.196	0.182 ± 0.178	0.118 ± 0.105	$\mathbf{0.102 \pm 0.093}$
MSE of FA ($\times 10^{-3}$)	2.52 ± 1.91	2.47 ± 1.88	1.55 ± 0.81	1.42 ± 0.79	$\mathbf{1.06 \pm 0.35}$

Table 4 shows a quantitative comparison of the performance of methods in a 3D tractography carried out in the region of interest (ROI) centered in the

corpus callosum, having the number of generated fibers (NGF) and the average length of tracts (ALT) as metrics. Figure 14 shows the graphical comparison of the same procedure. Visual and quantitative comparison demonstrates that it is possible to improve the fibers tracts reconstruction through interpolation of tensor fields.

Table 4: 3D Tractography metrics obtained by each interpolation method applied in the rank-2 real HOT field. NGF corresponds to the number of generated fibers and ALT is the average of length of tracts.

	NGF (Number)	Error NGF (%)	ALT(mm)	Error ALT (%)
Ground-Truth	2465	0	114.51	0
CDP	**2332**	**5.39**	113.66	0.74
TDP	2320	5.88	**113.85**	**0.58**
GWP	2236	9.29	112.6	1.67
Direct	1462	40.68	107.08	6.49
Log-Euclidean	1579	35.94	107.87	5.80
Raw-dMRI	1971	20.04	111.88	2.29

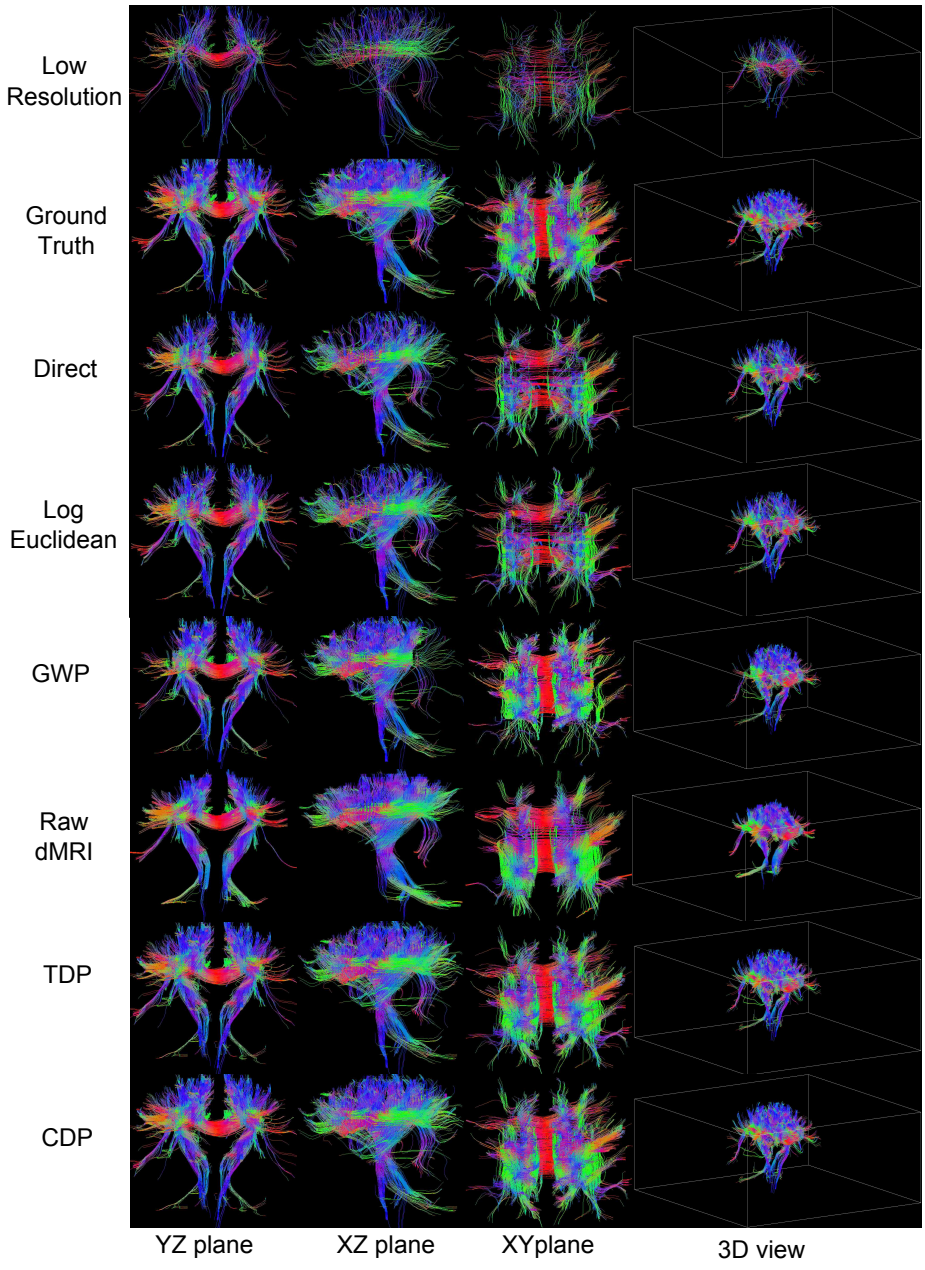

Figure 14: 3D tractography of the rank-2 dMRI field for the selected ROI centered in the corpus callosum. The reference is the ground-truth data. We show three cartesian planes and a 3D view.

3.4.2. Rank-4 and 6 results

Table 5 shows error results for HOT interpolation in rank-4 and 6 real dMRI data. Figures 15 and 16 illustrate the error map for rank-4 and the histogram of generalized anisotropy (GA) for rank-6, respectively. The TDP and CDP improve the performance when compared to linear interpolation and dMRI raw interpolation.

Table 5: Frobenius distance for rank-4 and 6 real HOT fields

	CDP	TDP	Raw dMRI	Direct interpolation
Rank-4	$\mathbf{1.178 \pm 1.025}$	1.320 ± 1.288	1.804 ± 0.978	2.739 ± 2.526
Rank-6	$\mathbf{3.211 \pm 2.923}$	3.492 ± 3.347	4.719 ± 2.547	6.243 ± 6.252

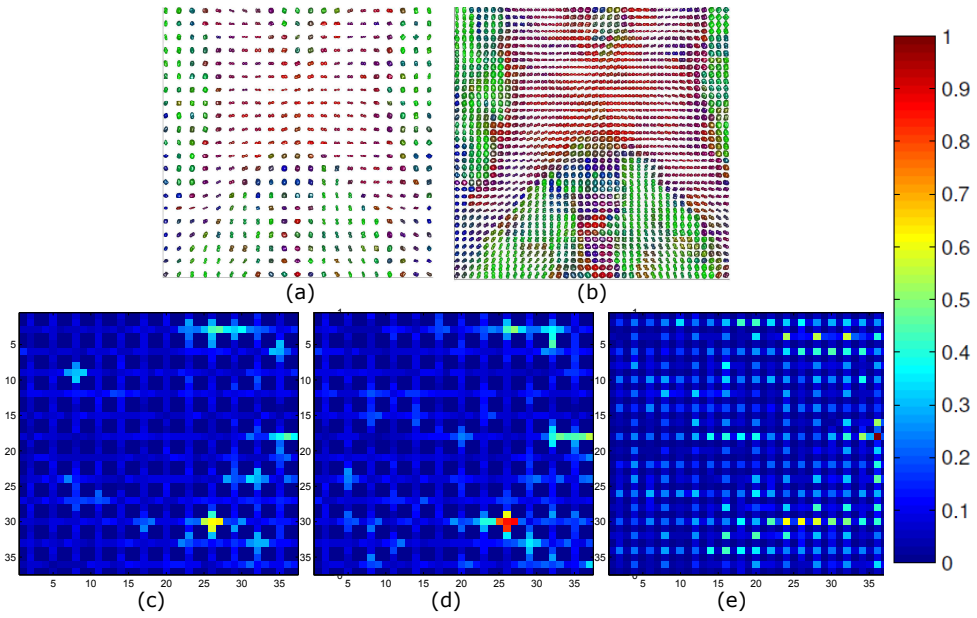

Figure 15: Normalized error maps for interpolation of rank-4 real HOT field: (a) Training data, (b) Ground-truth, (c) CDP, (d) TDP, (e) Raw dMRI

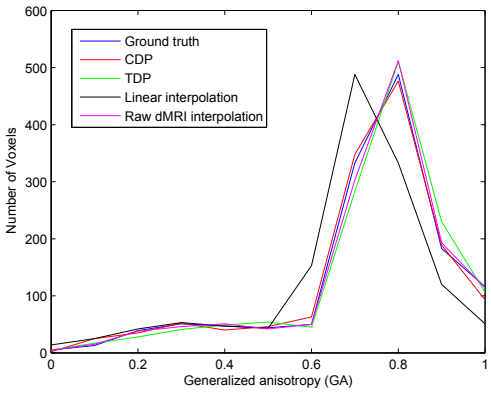

Figure 16: Generalized anisotropy (GA) curve for the rank-6 real dMRI HOT field

3.5. White matter (WM) segmentation

Table 6 and figure 17 show the white matter (WM) segmentation results. Our proposed methods outperform comparison approaches in synthetic, crossing fibers and real 2nd order fields, when we evaluate the Dice coefficient.

Table 6: Dice coefficient for white matter segmentation performed in synthetic, crossing fibers and real dMRI data.

	Direct interpolation	Log-Euclidean	GWP	TDP	CDP
Synthetic	0.964	0.917	0.961	0.974	**0.980**
Crossing fibers	0.958	0.953	0.963	0.982	**0.986**
Real dMRI	0.926	0.859	0.942	0.979	**0.981**

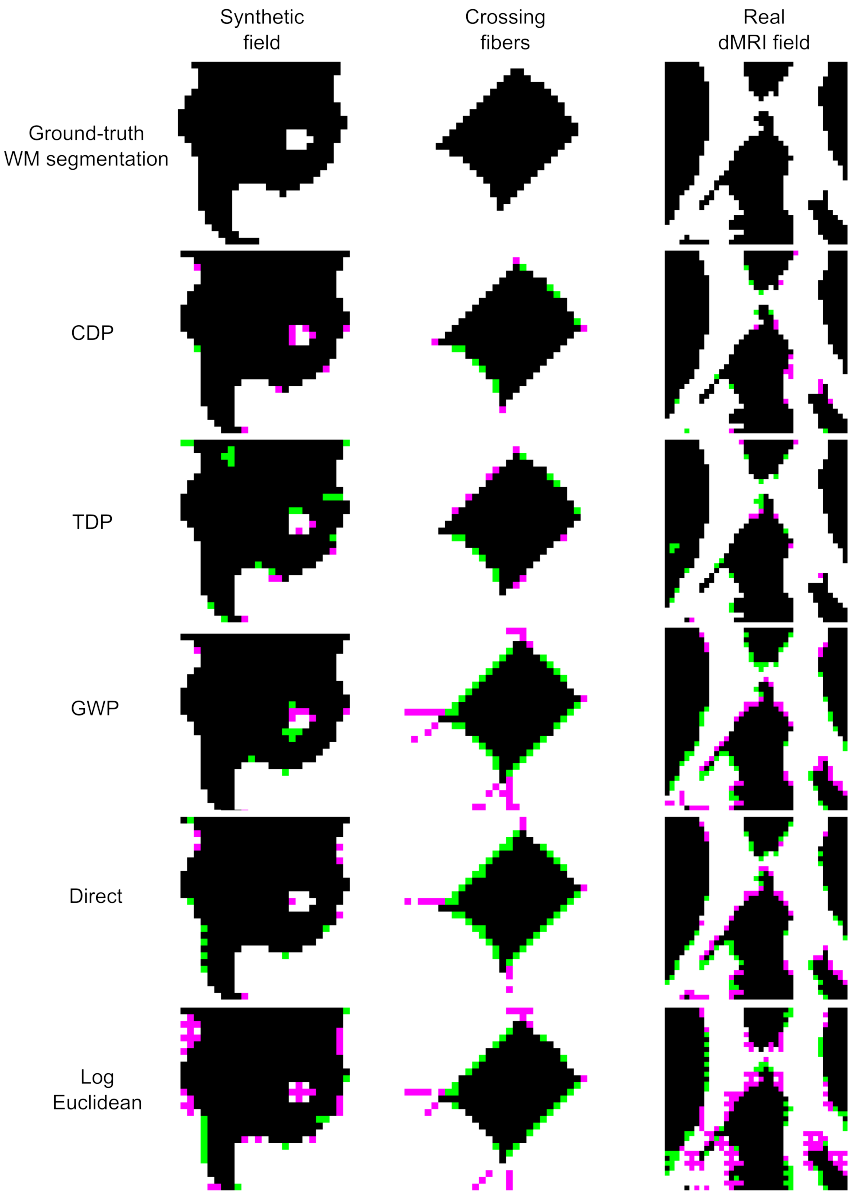

Figure 17: White matter (WM) segmentation results for synthetic, crossing fibers and real dMRI 2nd order fields. White voxels are WM, green and pink voxels correspond to false and positive negatives, respectively.

3.6. Computational time and ×4 Interpolation

Table 7 shows the time demanded for each algorithm during the interpolation of synthetic HOT fields (30×30 tensors).

Table 7: Computational times (in seconds) demanded for each algorithm. DNA: does not apply.

	Direct	Log-Euclidean	GWP	TDP	CDP
Rank-2	6.4	20.1	1528.2	2614.0	2469.2
Rank-4	7.6	DNA	DNA	3944.5	4963.7
Rank-6	8.9	DNA	DNA	66032.4	15243.9

Figure 18 illustrates the training data and ground-truth fields. Table 8 exhibits the Frobenius distance for ×4 interpolation experiments.

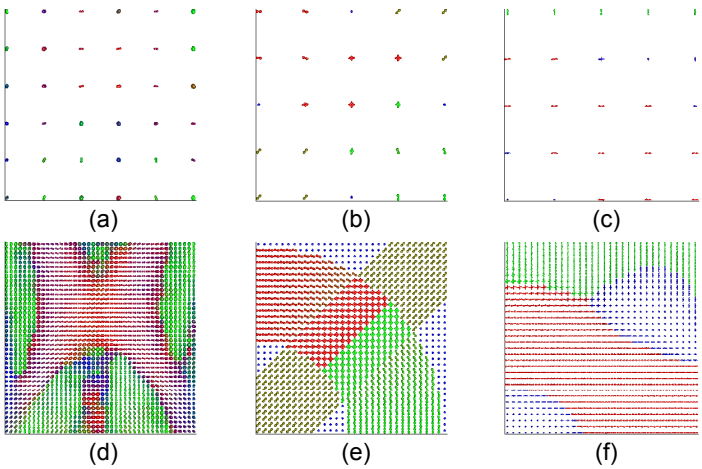

Figure 18: Training data and ground-truth fields for ×4 interpolation. (a), (b), (c) are the 2nd, 4th and 6th-order training data. (d), (e), (f), are the ground-truth fields.

Table 8: Frobenius distance for ×4 interpolation in rank-2, 4, 6 HOT fields. DNA: does not apply.

	Direct	Log-Euc	GWP	TDP	CDP
Real (rank-2)	0.796 ± 0.113	0.735 ± 0.266	1.167 ± 0.460	0.726 ± 0.236	$\mathbf{0.562 \pm 0.113}$
Crossing fibers (rank-4)	1.349 ± 0.948	DNA	DNA	1.353 ± 0.536	$\mathbf{1.115 \pm 0.468}$
Synthetic (Rank-6)	2.109 ± 0.678	DNA	DNA	2.234 ± 1.146	$\mathbf{1.969 \pm 0.855}$

3.7. Discussion

The proposed approaches (CDP and TDP) demonstrate better performance in interpolation of HOT fields of 2nd, 4th, and 6th-order, compared to direct linear interpolation and dMRI raw interpolation. In rank-2 data, the CDP and TDP also outperform log-Euclidean interpolation and the recently proposed framework based on generalized Wishart processes (Vargas Cardona et al., 2015). Our methods are adaptive to different type of data. Thus, they can capture the global spatial trend of smooth fields or deliver precise estimation among neighboring tensors. The CDP and TDP are flexible to model several transitions inside HOT fields. This property is important because HOT data are very heterogeneous. Quantitative results of Frobenius distance presented in tables 1, 2, 3, 5 show that the CDP and TDP always outperform the compared methods, for each dataset and for any order. The accuracy in estimation of new data is mandatory for interpolation of HOT data. Another key factor is that the proposed methods ensure positive definite tensors.

The Rician noise analysis is very useful for probing robustness of the CDP and TDP. Diagrams of mean error and standard deviation of figures 7, 9 show a better performance of CDP and TDP than the state of the art approaches. If we compare CDP and TDP each other, both methods obtain statistically similar results. This behavior remains constant for all evaluated cases of SNR levels (including an extreme case of SNR=1) and different tensor orders. Robustness to noise of CDP and TDP is due to probabilistic modeling (Gaussian processes) of their parameters. The GPs modulate those parameters considering the tensors as noisy data. Therefore, there is an assumption of intrinsic noise in the model. Unlike classical deterministic interpolation, a probabilistic inference methodology is not highly affected when the training data are corrupted by noise. We must consider that brain dMRI data are always altered by Rician noise and different artifacts added in acquisition procedure.

Qualitative results of figures 10, 11. 13, 15 illustrate an interesting behavior when there are strong changes among nearby tensors. Looking at the figures in detail, the traditional methods can not capture accurately the rapid transitions

in the field, no matter the rank. The most extreme case is the crossing fibers fields (figures 10, 11). These strong changes in spatial dynamic of HOT fields are very difficult to follow, even for robust methods. The CDP and TDP capture these changes with low error. For example the direct transition from blue to green tensors, when they are highly anisotropic. Probabilistic models presented in this work adapt much better to abrupt changes compared to the other methods. Another remarkable aspect of the proposed approaches is the guarantee of positive definite (PD) tensors. For this reason, the estimated data are physically realizable. Some methods such as linear direct interpolation and log-Euclidean can not ensure the estimation of PD tensors in noisy data, i.e. the real dMRI dataset. MSE of FA displayed in tables 1, 3 demonstrate that probabilistic approaches for tensorial interpolation are robust and can preserve morphological properties relevant in clinical applications. Again, outcomes for CDP and TDP are better than the comparison methods in all experiments.

3D tractography results exhibited in table 4 and figure 14 are particularly relevant to remark the pertinence of reducing voxel size in HOT fields. Regarding this, interpolation of tensor data allows to highlight anatomical details that can be seen only in very high resolution acquisitions. We consider that a HOT study with enhanced spatial resolution can improve the quality of tractography and aids the mapping of tissue structures. If we observe, the fiber tracts reconstructed from low resolution data (see first row of figure 14) is poorer than the reconstruction from high resolution data (second row of figure 14), where the density and number of fibers is clearly inferior in the corpus callosum and surrounding regions. Additionally, interpolation of the HOT fields reveals more fined structural features of complex fiber bundles (i.e. crossing and bifurcated fibers), improves the representation of tract shapes, and it augments the contrast in tissue boundaries. Furthermore, segmentation of gray matter (GM) and white matter (WM) is easier from FA maps, because of the increased contrast. In this sense, enhancing spatial resolution of HOT data takes relevance in clinical applications. For example; the surgical planning, where tractography is employed to map the displacements of projecting tracts and low resolution scans' insufficient

accuracy can cause difficulties in this procedure (Dirby et al., 2014). Also, the preliminary diagnosis of tumorous, ischemic or inflammatory lesions of the spinal cord (Vargas et al., 2008), where it is required high resolution visual data.

In agreement with quantitative results of table 4, the CDP and TDP achieve tractography metrics close to the ground-truth study (the selected ROI has a size of $40 \times 40 \times 10$ voxels, centered in the corpus callosum). In this case we evaluate the number of generated fibers (NGF) and the average length of tracts (ALT). The GWP and dMRI-raw interpolation obtain acceptable results, while the deterministic methods (direct and log-Euclidean) have the lower performance. Qualitative results of fiber reconstruction (see figure 14) show missing fibers and a considerable reduction of the fiber density in some regions for direct and log-Euclidean approaches. Moreover, we observe a smoothing of fiber tracts that generates a contrast loss for dMRI-raw interpolation; the problem of this blurring effect is that tiny brain structures and edges tend to disappear. As we explained before, proposed methods interpolate the tensors with low error and obtain tractography metrics nearby to the gold-standard. Summarizing, when we employ probabilistic methodologies for interpolation of tensor data, it is possible to get accurate 3D tractographic reconstruction from post processed low resolution dMRI scans.

Generalized anisotropy is an extension of FA for rank-4 and 6. The GA curves (figures 12, 16) obtained for the proposed methods follow the trend of the ground truth, especially the CDP. It means that interpolation of HOT with CDP or TDP does not affect the intrinsic physiological information of dMRI. While, the linear interpolation can not retain the trends in high values of GA (from 0.8 to 1.0). multiple crossings (i.e crossing fibers) in HOT fields occur in anisotropic regions. In consequence, linear interpolation is not able to capture with good accuracy the complex tissue structures. The method of Raw dMRI interpolation tested only in the real dataset, can keep the GA tendency. However, it generates swelling effect in the estimated tensors.

CDP and TDP are Bayesian models whose parameters are modeled with Gaussian processes. Due to the probabilistic nature of CDP and TDP, it is not

possible to achieve an analytical solution for the posterior distribution. It is necessary to employ Markov Chain Monte Carlo methods for finding the posterior (elliptical slice sampling and Metropolis Hastings). There is a bottleneck in the construction of tensors with Tucker or canonical decomposition, when we calculate Kronecker products. A feasible option is to employ *mode-n* products. However, this procedure demands more operations and loops. Therefore, computational cost of CDP and TDP increases considerably with the number of training data. As we pointed out before, we split the entire field in several subfields and we employ a patch-based scheme. Then, we execute the algorithms at the same time, improving the performance and reducing the time needed for a successful training.

An important aspect that must be taken into account is the slow convergence of the MCMC methods used in our framework. This issue is critical for a large number of voxels in training data, because the time demanded to complete the training stage increases considerably. For this reason, we split the entire field in subfields that we process simultaneously. Also, it is necessary to employ dynamic patches into each subfield (i.e. 3×3 for enhancing to 5×5).

When we make a direct comparison between CDP and TDP, we do not find statistically significant differences in their outcomes, no matter the rank or dataset. We can say both methods have a comparable performance under any condition. Intuitively, we think this identical performance of CDP and TDP is due to their similar mathematical construction based on outer products, taking account that parameters of CDP are scaled-vectors and parameters of TDP are matrices and a core tensor. Also, the MCMC-based learning stage is almost the same for them. In relation to the convergence of each proposed method, we observe that time of training stage of CDP is more affected by the tensor rank than TDP. As we explained before, the size of matrices of TDP does not depend on the rank, while the number of vectors and eigenvalues in CDP increases considerably for higher orders. For example, in rank-2 fields, the learning stage of CDP is faster than TDP. For rank-4 is similar. However, for rank-6 tensors there is a considerable difference in favor of TDP. According to this, we consider

that CDP is a suitable approach for lower ranks (2 and 4), and TDP is the appropriated method for higher orders (6 or more).

White matter (WM) segmentation results of table 6 and figure 17 illustrate another advantage of our framework. Both CDP and TDP achieve high accuracy in WM segmentation, obtaining a low number of false positives or negatives, and a Dice coefficient near to one. We think a probabilistic modeling allows to keep the main characteristics of physiological information contained in a dMRI study, such as the WM tissue and anisotropy descriptors.

We measure the time demanded for each algorithm during the interpolation of synthetic data in tensor fields of several orders. Results of table 7 make evident that execution times in probabilistic approaches (CDP, TDP, GWP) are considerably higher than the baseline methods. Currently, the computational cost of CDP and TDP is the main bottleneck of the proposed framework. Future work includes using Gaussian Processes for Big Data Hensman et al. (2013) to reduce computational complexity.

Finally, we evaluate a $\times 4$ interpolation for the same datasets. Results of table 8 demonstrate that CDP obtains the best error and has a better generalization capability than TDP. Also, linear interpolation is an acceptable approach for estimating new tensors with a few amount of training data.

4. Conclusions and future work

In this paper, we presented two methods for tensorial interpolation of diffusion magnetic resonance imaging: the canonical decomposition process (CDP) and the Tucker decomposition process (TDP). The proposed methods generalize to higher order tensors, in contrast to traditional methods presented in the state of the art, valid only for rank-2 tensors. The canonical and the Tucker process outperformed the linear method, log-Euclidean, Generalized Wishart processes, and dMRI raw interpolation, when we tested three different datasets and for tensor fields of rank-2, 4 and 6.

Also, we performed a morphological validation. For rank-2 tensor fields we

evaluated fractional anisotropy (FA) maps and tractography (2D and 3D). For rank-4 and 6 tensors, we obtained the generalized anisotropy (GA) histograms. CDP and TDP can preserve morphological properties of dMRI, avoiding non positive definite tensors and the swelling effect. For HOT data, it was possible to achieve high accuracy in GA curves, even in anisotropic regions.

CDP and TDP are Bayesian models, where their parameters are defined by a set of Gaussian processes. The probabilistic nature of proposed approaches favored the robustness, flexibility, generalization capability, and adaptability to heterogeneous or noisy data. On the other hand, the comparison methods reduced considerably their performance in presence of high levels of Rician noise.

Future work includes using Gaussian Processes for Big Data Hensman et al. (2013) to reduce computational complexity.

5. Acknowledgments

H. D. Vargas-Cardona is funded by Colciencias under the program: formación de alto nivel para la ciencia, la tecnología y la innovación - Convocatoria 617 de 2013. M. Á. Álvarez has been partially supported by the Engineering and Physical Research Council (EPSRC) Research Project EP/N014162/1. This research is developed under the project: *Desarrollo de un sistema de soporte clínico basado en el procesamiento estocástico para mejorar la resolución espacial de la resonancia magnética estructural y de difusión con aplicación al procedimiento de ablación de tumores*, financed by Colciencias with code 111074455860. Data collection and sharing for this project was provided by the MGH-USC Human Connectome Project (HCP; Principal Investigators: Bruce Rosen, M.D., Ph.D., Arthur W. Toga, Ph.D., Van J. Weeden, MD). HCP funding was provided by the National Institute of Dental and Craniofacial Research (NIDCR), the National Institute of Mental Health (NIMH), and the National Institute of Neurological Disorders and Stroke (NINDS). HCP data are disseminated by the Laboratory of Neuro Imaging at the University of California, Los Angeles.

References

Alvarez, M., & Lawrence, N. (2011). Computationally efficient convolved multiple output Gaussian processes. *Journal of Machine Learning Research*, *12*, 1459–1500.

Arsigny, V., Fillard, P., Pennec, X., & Ayache, N. (2006). Log-Euclidean metrics for fast and simple calculus on diffusion tensors. *Magn. Reson. Med.*, *56*, 411–421.

Astola, L., & Florack, L. (2009). Finsler geometry on higher order tensor fields and applications to high angular resolution diffusion imaging. *Lecture Notes on Computer Science*, *5567*, 224–234.

Astola, L., Jalba, A., Balmashnova, E., & Florack, L. (2011). Finsler streamline tracking with single tensor orientation distribution function for high angular resolution diffusion imaging. *J Math Imaging Vis.*, *41*, 170–181.

Barmpoutis, A., & Vemuri, B. (2010). A unified framework for estimating diffusion tensors of any order with symmetric positive-definite constraints. In *Proceedings of ISBI10: IEEE International Symposium on Biomedical Imaging* (pp. 1385–1388).

Barmpoutis, A., Vemuri, B., Shepherd, T., & Forder, J. (2007). Tensor splines for interpolation and approximation of DT-MRI with applications to segmentation of isolated rat hippocampi. *IEEE Trans. On Medical Imaging*, *26*, 1537–1546.

Basser, P., Mattiello, R., & Le Bihan, D. (1993). Diffusion tensor echo-planar imaging of human brain. In *Proceedings of the SMRM* (pp. 584–562). volume 56.

Basser, P., Mattielo, R., & Le Bihan, D. (1994). Estimation of the effective self-diffusion tensor from the NMR spin echo. *J. Magn. Reson.*, *103*, 247–254.

Berman, J., Lanza, M., Blaskey, L., Edgar, J., & Roberts, T. (2013). High angular resolution diffusion imaging probabilistic tractography of the auditory radiation. *American Journal of Neuroradiology*, *34*, 1573–1578.

Butson, C., Maks, C., Walter, B., Vitek, J., & McIntyre, C. (2007). Patient-specific analysis of the volume of tissue activated during deep brain stimulation. *Neuroimage*, *34*, 661–670.

Carroll, J., & Chang, J. (1970). Analysis of individual differences in multidimensional scaling via n-way generalization of Eckart-Young decomposition. *Psychometrika*, *35*, 283–319.

Comon, P., Golub, G., Lim, L.-H., & Mourrain, B. (2008). Symmetric tensors and symmetric tensor rank. *SIAM Journal on Matrix Analysis and Applications*, *30*, 1254–1279.

Dirby, T., Lundell, H., Burke, M., Reislev, N., Paulsona, O., Ptito, M., & Siebner, H. (2014). Interpolation of diffusion weighted imaging datasets. *Neuroimage*, *103*, 202–213.

Fletcher, P., & Joshi, S. (2007). Riemannian geometry for the statistical analysis of diffusion tensor data. *Signal Processing*, *87*, 250–262.

Gulliksen, H., & Frederiksen, N. (Eds.) (1964). *Contributions to mathematical psychology*. New York: Holt, Rinehart and Winston.

Harshman, R. (1970). Foundations of the parafac procedure: Models and conditions for an explanatory multimodal factor analysis. *UCLA Working Papers in Phonetics*, *16*, 1–84.

Hasan, K., Gupta, R., Santos, R., Wolinsky, J., & Narayana, P. (2005). Diffusion tensor fractional anisotropy of the normal-appearing seven segments of the corpus callosum in healthy adults and relapsing-remitting multiple sclerosis patients. *J. Magn. Reson. Imag*, *21*, 735–743.

Hensman, J., Fusi, N., & Lawrence, N. D. (2013). Gaussian processes for big data. *CoRR*, *abs/1309.6835*. URL: `http://dblp.uni-trier.de/db/journals/corr/corr1309.html#HensmanFL13`.

Kindlmann, G., Estepar, R., Niethammer, M., Haker, S., & Westin, C. (2007). Geodesic-loxodromes for diffusion tensor interpolation and difference measurement. *Signal Processing*, *10*, 1–9.

Liu, C., Bammer, R., Acar, B., & Moseley, M. (2004). Characterizing non-Gaussian diffusion by using generalized diffusion tensors. *Magnetic Resonance in Medicine*, *51*, 924–937.

Mackay, D. (1998). Introduction to gaussian processes. *Computer and Systems sciences*, *168*, 133–166.

Moakher, M. (2008). Fourth-order cartesian tensors: old and new facts, notions and applications. *The Quarterly Journal of Mechanics and Applied Mathematics*, *61*, 181–203.

Mori, S., Crain, B., Chacko, V., & van Zijl, P. (1999). Three-dimensional tracking of axonal projections in the brain by magnetic resonance imaging. *Ann Neurol*, *45*, 265–269.

Murray, I., Adams, R., & Mackay, D. (2010). Elliptical slice sampling. *JMLR*, *9*, 541–548.

Nath, K., Husain, M., Trivedi, R., Kumar, R., Prasad, K., Rathore, R., & Gupta, R. (2007). Clinical implications of increased fractional anisotropy in meningitis associated with brain abscess. *J. Comput. Assist. Tomogr*, *31*, 888–893.

Ozarslan, E., & Mareci, T. (2003). Generalized diffusion tensor imaging and analytical relationships between diffusion tensor imaging and high angular resolution diffusion imaging. *Magnetic Resonance in Medicine*, *50*, 955–965.

Pajevic, S., Aldroubi, A., & Basser, P. (2002). A continuous tensor field approximation of discrete DT-MRI data for extracting microstructural and architectural features of tissue. *J. Magn. Reson.*, *154*, 85–100.

Pennec, X., Fillard, P., & Ayache, N. (2006). A Riemannian framework for tensor computing. *International Journal of Computer Vision*, *66*, 41–66.

Ptak, T., Sheridan, R., Rhea, J., Gervasini, A., Yun, J., Curran, M., Borszuk, P., Petrovick, L., & Novelline, R. (2003). Cerebral fractional anisotropy score in trauma patients: a new indicator of white matter injury after trauma. *AJR Am. J. Roentgenol*, *181*, 1401–1407.

Qi, L., Wang, F., & Wang, Y. (2009). Z-eigenvalue methods for a global polynomial optimization problem. *Mathematical Programming*, *118*, 301–316.

Rasmussen, C. E., & Williams, C. K. I. (2006). *Gaussian Processes for Machine Learning*. Cambridge, MA: The MIT Press.

Robert, C. P., & Casella, G. (2005). *Monte Carlo Statistical Methods (Springer Texts in Statistics)*. Secaucus, NJ, USA: Springer-Verlag New York, Inc.

Shi, J., & Malik, J. (2000). Normalized cuts and image segmentation. *IEEE TRANSACTIONS ON PATTERN ANALYSIS AND MACHINE INTELLIGENCE*, *22*, 888–905.

Vargas, M., Delavelle, J., Jlassi, H., Rilliet, B., Viallon, M., Becker, C., & Lovblad, K. (2008). Clinical applications of diffusion tensor tractography of the spinal cord. *Neuroradiology*, *50*, 25–29.

Vargas Cardona, H., Alvarez, M., & Orozco, A. (2015). Generalized Wishart processes for interpolation over diffusion tensor fields. *Lecture Notes in Computer Science*, *9475*, 499–508.

Yang, F., Zhu, Y., Luo, J., Robini, M., Liu, J., & Croisille, P. (2014). A comparative study of different level interpolations for improving spatial resolution in diffusion tensor imaging. *IEEE Journal of Biomedical and Health Informatics*, *18*, 1317–1327.

Yang, F., Zhu, Y., Magnin, I., Luo, J., Croisille, P., & Kingsley, P. (2012). Feature-based interpolation of diffusion tensor fields and application to human cardiac DT-MRI. *Medical Image Analysis*, *16*, 459–481.

Yassine, I., & McGraw, T. (2008). A subdivision approach to tensor field interpolation. In *Workshop On Computational Diffusion MRI* (pp. 117–124).

Yassine, I., & McGraw, T. (2009). 4th order diffusion tensor interpolation with divergence and curl constrained bezier patches. In *Proceedings of ISBI09: IEEE International Symposium on Biomedical Imaging* (pp. 634–637).